Study of the magnetoelastic effect in nickel and cobalt thin films at GHz range using x-ray microscopy

Marc Rovirola [1,2,*] M. Waqas Khaliq [1,3,†] Travis Gustafson,[4] Fiona Sosa-Barth,[1] Blai Casals [2,5]
Joan Manel Hernàndez [1,2] Sandra Ruiz-Gómez [6] Miguel Angel Niño,[3] Lucía Aballe [3] Alberto Hernández-Mínguez [7]
Michael Foerster [3] and Ferran Macià [1,2,‡]

[1]*Department of Condensed Matter Physics, University of Barcelona, 08028 Barcelona, Spain*
[2]*Institute of Nanoscience and Nanotechnology (IN2UB), University of Barcelona, 08028 Barcelona, Spain*
[3]*ALBA Synchrotron Light Source, 08290 Cerdanyola del Vallès, Spain*
[4]*Department of Physics, Norwegian University of Science and Technology (NTNU), 7034 Trondheim, Norway*
[5]*Department of Applied Physics, University of Barcelona, 08028 Barcelona, Spain*
[6]*Max Planck Institute for Chemical Physics of Solids, 01187-Dresden, Germany*
[7]*Paul-Drude-Institut für Festkörperelektronik, Leibniz-Institut im Forschungsverbund Berlin e.V., 10117 Berlin, Germany*

We use surface acoustic waves of 1 and 3 GHz in hybrid piezoelectric-magnetic systems with either nickel or cobalt as a magnetic layer to generate magnetoacoustic waves and directly image them using stroboscopic x-ray magnetic circular dichroism imaging. Our measurements visualize and quantify the amplitudes of both acoustic and magnetic components of the magnetoacoustic waves, which are generated in the ferromagnetic layer and can propagate over millimeter distances. Additionally, we quantified the magnetoelastic strain component for nickel and cobalt through micromagnetic simulations.

I. INTRODUCTION

There is an increasing interest in manipulating magnetization dynamics to create low-power consumption devices capable of transmitting and encoding information efficiently [1]. A challenge lies in effectively creating and controlling magnetic excitations in nanodevices. The most common way to manipulate magnetization typically involves the use of magnetic fields. However, this approach has several downsides, including issues with nonlocality, and challenges with integrating controllable magnetic fields into micrometer-scale devices. Other approaches explore interactions of conducting electron's spin [2,3], lattice phonons [4,5], or ultrashort light pulses [6] with magnetic excitations. Promising alternatives have been proposed, such as the use of strain. The field of straintronics [4] studies strain-induced effects in solids and special attention is directed to magnetic materials as a promising alternative for reduced energy-consumption devices [7]. Strain couples to magnetic states through the magnetoelastic (ME) effect, which is the change of magnetic properties due to mechanical deformation. This effect has already been proposed and used in many applications [5] including the reversing magnetization of patterned nanomagnets [8,9] or inducing a phase transition from antiferromagnetic ordering to ferromagnetic ordering [10].

The ME effect can be used to generate spin waves—collective excitations of magnetic order—through surface acoustic waves (SAWs) [11,12], which are strain waves propagating at the surface of a solid. SAWs generate an oscillating strain in both space and time which can create an oscillating magnetic anisotropy field on a magnetostrictive material [13,14]. This dynamic anisotropy field may induce a magnetization variation with the same wavelength and frequency as the SAWs and the excitation may propagate up to millimeter distances [15]. These hybrid waves are referred to as magnetoacoustic waves (MAWs) and have been studied in a wide range of materials by measuring acoustic attenuation as a function of the magnetic state [16–20] or by direct imaging using magneto-optic Kerr effect (MOKE) [20,21] or x-ray magnetic circular dichroism (XMCD) [15,22]. Using the same principles, more recently also Néel vector waves have been observed in antiferromagnetic CuMnAs [23] by x-ray linear dichroism (XLD).

SAWs are typically generated using interdigital transducers (IDTs) deposited on piezoelectric substrates [24]. IDTs are interlocking arrays of metallic electrodes that can excite SAWs up to GHz frequencies. IDTs are used in electronics as radio frequency delay lines and filters and their integration into micrometric devices is well established [25]. SAW-based technology can be efficiently integrated into low-power devices since the SAW amplitude depends on the amplitude of the oscillating voltage applied to the IDT instead of the current.

*marc.rovirola@ub.edu
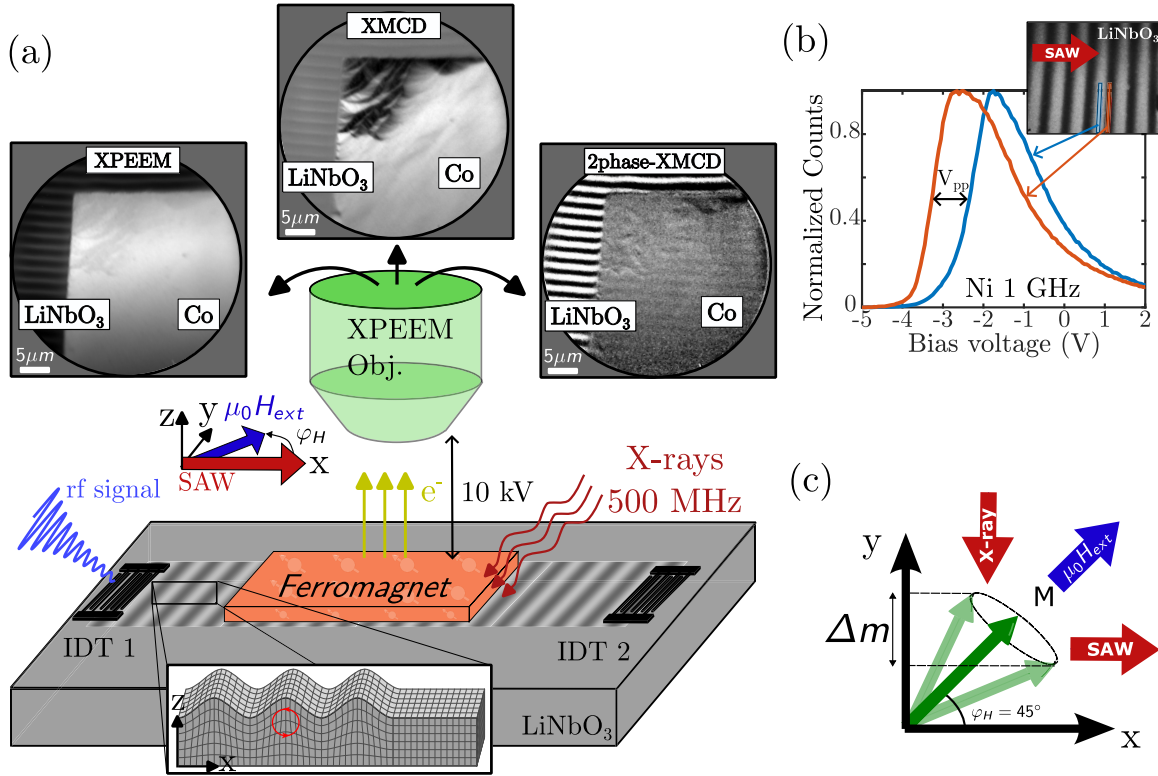†mkhaliq@cells.es
‡ferran.macia@ub.edu

FIG. 1. (a) Schematic of the experimental setup. A thin film of either Ni or Co is grown in the middle of the acoustic path (*x-y* plane), where SAW propagate along the *x* direction. The Co sample can only be excited at 1 GHz by either IDT. The microscope (XPEEM Objective) is operated at 10 kV with respect to the sample to accelerate low energy electrons kicked out by the x rays (which are applied along the *y* axis). From this setup, we can obtain XPEEM and XMCD images. The magnetic field is applied in-plane at an angle $\varphi_H = 45°$ relative to the SAW propagation direction. (b) Local photoelectron energy spectra measured at opposite SAW phases (tensile and compressive). The orange line represents the dark SAW phase, while the blue line represents the bright SAW phase. The *x* axis depicts the bias voltage applied between the sample and the XPEEM objective; voltage shift between both spectra corresponds to the peak-to-peak SAW piezoelectric voltage, V_{pp}. (c) Representation of the direction of SAW (*x* direction), magnetic field (45°), and x ray (*y* direction). In this experiment, the SAW and x ray are perpendicular to each other. The horizontal dashed lines represent the change in magnetization projection captured with the x rays.

Magnetic imaging techniques based on MOKE [26,27] or XMCD [15,22,28] provide the opportunity to directly measure MAWs and thus study the effect of the coupling between strain and spin waves in both space and time. Recent experiments have shown that the ME effect is as efficient in dynamic processes up to 500 MHz as in static processes [28], thus fueling the idea of using SAWs in magnonic applications. Furthermore, experiments on Fe$_3$Si with cubic anisotropy revealed both resonant and nonresonant MAWs [22] with a noticeable increase in amplitude at resonance. There is thus a need for working at the GHz frequency range where most ferromagnets have internal resonances and where miniaturization of MAWs might meet the requirements for modern technologies [25].

In this paper, we study MAWs at 1 and 3 GHz in nickel (Ni) and MAWs at 1 GHz in cobalt (Co) using stroboscopic x-ray photoemission electron microscopy (XPEEM) combined with XMCD imaging. Our analysis reveals that both Ni and Co exhibit MAWs across a wide range of magnetic fields, with each material displaying different profiles and amplitudes. With the help of micromagnetic simulations, we are able to quantify the strength of the magnetoelastic coupling for both magnetic materials at the studied frequencies.

II. EXPERIMENTAL METHODS

Thin films of polycristalline Ni and Co with a thickness of 20 nm were grown on the acoustic path of several SAW delay lines by e-beam evaporation. The samples exhibit an in-plane anisotropy with a magnetization saturation of 490 kA/m^3 for Ni and 1510 kA/m^3 for Co. The delay lines consist of pairs of unidirectional IDTs deposited on piezoelectric lithium niobate (128Y-cut LiNbO$_3$) substrates; see Fig. 1. The IDTs are designed to generate SAWs with frequencies of 1 GHz and 3 GHz for the Ni sample and only 1 GHz for the Co sample. These frequencies are conveniently selected to match the synchrotron repetition rate (499.654 MHz), thus allowing for stroboscopic images. To generate SAWs, we excite the IDTs with an oscillating electrical signal of the appropriate frequency that is transformed into strain through the inverse piezoelectric effect [11]. Notice that SAWs are limited to a substrate depth of the order of the SAW wavelength [29], corresponding to 3.8 μm and 1.26 μm for 1 and 3 GHz, respectively. Within this depth region, the SAW causes a periodic modulation of the crystal lattice in the substrate and on any thin film deposited on its surface. If the thin film is magnetostrictive, then the periodic displacement of atoms caused by the SAWs produces a periodic effective magnetic field in

the thin film as a result of the inverse magnetostrictive effect, commonly referred to as the ME effect.

The experiment was performed at the XPEEM experimental station of the ALBA Synchrotron Light Facility [30]. A schematic representation of the setup is shown in Fig. 1(a). SAWs are emitted in the x direction and are synchronized with the repetition rate of the synchrotron x-ray bunches. This synchronization allows for stroboscopic images at a particular phase of the SAWs. The x rays from the synchrotron are directed onto the sample, knocking out secondary electrons (called photoelectrons). These photoelectrons are then pulled out of the sample by a 10 kV potential difference between the XPEEM objective and the sample. The kinetic energy of these photoelectrons is sensitive to the electrical field at the sample surface. By adjusting a bias voltage at the detector we can scan the photoelectron energy spectrum at the sample surface. Figure 1(b) shows the photoelectron energy spectra at different SAW phases. The shift in energy between phases is directly related to the electric potential generated by the SAWs. However, the metallic nature of the thin films of Ni and Co shields the piezoelectric field within the first nanometers at the bottom of the film and therefore the SAW's electric potential vanishes at the film's top surface. To obtain magnetic contrast, two XPEEM images with opposite circular light polarization (circular left and circular right) are subtracted to obtain an XMCD image. The energy of the x rays is specifically chosen at the L_3 edge of Ni and Co to provide information about the electrons responsible for the magnetization. More details on synchronized SAW stroboscopic XPEEM measurements and the upgraded setup to support >500 MHz excitations can be found elsewhere [31,32]. The insets of Fig. 1(a) display the three imaging modalities of the setup. The top-left corner depicts an XPEEM image with clear SAWs contrast on the LiNbO$_3$, accompanied by a weak contrast of magnetic domains on the Co. The top-center depicts an XMCD image that highlights the magnetic contrast on the Co magnetic domains, accompanied by faint traces of residual SAWs on the LiNbO$_3$ due to thermal drifts in subsequent images (and thus slightly different SAW propagation velocities). The top-right corner depicts a two-phase-XMCD image, which consists of capturing two XPEEM images with a 180-phase shift in SAW for each x-ray helicity, followed by a subtraction between both phases and helicities. This method enhanced both the magnetic and piezoelectric contrast while eliminating static contrast such as magnetic domains, enabling a clearer measurement of MAWs. Figure 1(b) illustrates the local spectra detector counts for Ni at 1 GHz plotted against the bias voltage, which is applied between the sample and the XPEEM objective, at opposite SAW phases, highlighted in orange and blue. The voltage shift between both spectra (V_{pp}) corresponds to the peak-to-peak amplitude of the SAW piezoelectric potential at the surface of the LiNbO3 substrate. Figure 1(c) shows the directions of the SAW, the magnetic field, and the x rays. The SAW and the magnetic field are at about 45° with respect to each other to exert maximum magnetoelastic torque [33], whereas the SAW and x rays are perpendicular to each other in order to detect the magnetization changes in the y direction as represented by the dashed lines in Fig. 1(c).

III. RESULTS

An initial characterization of the samples was performed to study the angular dependence of their acoustic-ferromagnetic resonance (a-FMR) at 1 GHz. The experiment consists of placing our hybrid device [see Fig. 1(a)] between the poles of an electromagnet and measuring the transmitted acoustic signal between IDT1 and IDT2, S_{21}, with a vector network analyzer at different angles between the SAWs and the in-plane magnetic field. In contrast to FMR, where an rf-magnetic field is used to drive the magnetization into resonance, a-FMR uses the periodic strain field of the SAW to induce magnetization precession by modulating the effective magnetic field of the sample. Additionally, the nonzero wave vector of the SAW must be taken into account in the determination of the resonance magnetic fields and frequencies [17].

The coupling between magnetization and SAWs can generate MAWs under certain conditions of the external magnetic field. At resonance, significant energy is transferred from the SAW to the magnetic system, resulting in SAW attenuation and phase shift that are detected in the S_{21} measurement [16]. The SAW attenuation as a function of the magnitude and angle of the applied magnetic field (in both cases, the magnetic field was swept from negative to positive values) is presented in Fig. 2. In both samples, a large attenuation is observed, regardless of the angle, at a fixed magnetic field that corresponds to the magnetization-switching field of the film. In addition, Ni [Fig. 2(a)] shows the typical fourfold shape with large attenuation between ±30° and ±50° and a maximum around 45° where the ME torque is the largest [16,33,34]. As the angle between SAW and the magnetic field exceeds 50° or drops below 30°, the attenuation decreases, reaching the minimum ME torque at 0° and 90°. In contrast, the SAW attenuation for Co [Fig. 2(b)] is strongest at magnetic field angles between −30° and 30°, above which the attenuation rapidly decays. Similar results for Co can be found in Ref. [35]. We can see an asymmetric attenuation in the Co sample for both positive and negative fields and positive and negative angles. This nonreciprocal behavior is typically determined by the effective magnetic fields associated with the SAW due to the magnetoelastic and magnetorotation couplings [36–38]. Insets in Figs. 2(a) and 2(b) show S_{21} attenuation at representative angles, where the nonreciprocal effect can be observed, especially for the Co sample.

Prior to capturing XMCD images of the magnetization, the IDTs are tested by measuring the amplitude of the SAW piezoelectric potential according to the method shown in Fig. 1(b). By solving the coupled elastic and electromagnetic equations, we can obtain the amplitude of the strain components, e_{xx}, e_{xz}, and e_{zz}, associated with the SAW images [39,40]. It is important to note that the strain components may vary depending on SAW frequency. Thus we measured the strain component in each sample at the same SAW excitation frequency and power that are employed for the XMCD imaging (see Table I).

In the following sections, we show the results obtained from the XMCD imaging and discuss the amplitude of the MAWs for the different samples and excitation frequencies. To normalize the MAW amplitude, we determine the M_s in units of XMCD contrast from an XMCD image featuring magnetic domains [see Fig. 1(a)]. The contrast difference
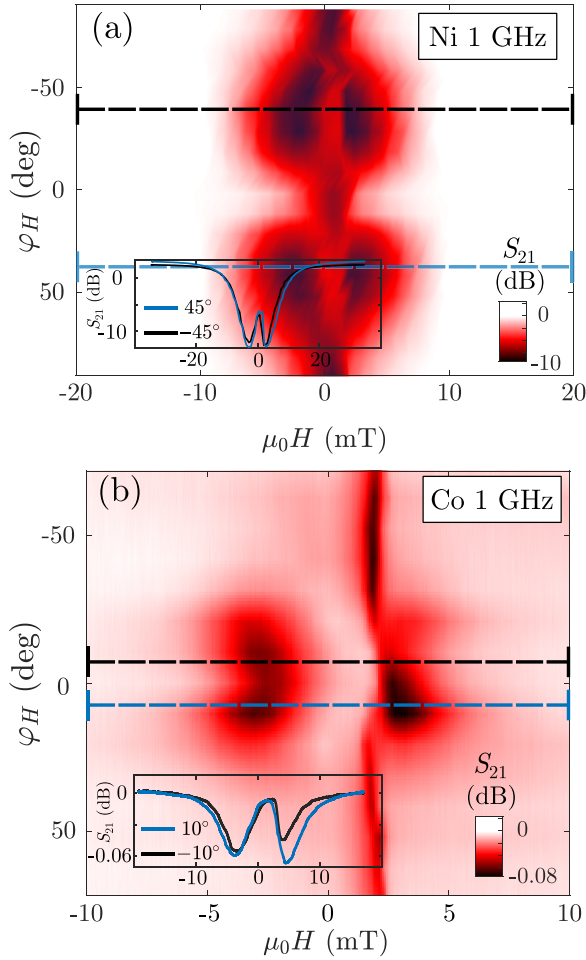
FIG. 2. (a) Ni S_{21} attenuation at 1 GHz for several angles between the SAW and the magnetic field showing different absorption values with a maximum close to 45° and minimums at 0° and above 60°. The inset shows a horizontal cut of S_{21} attenuation for $\varphi_H = 40°$ (black curve) and $\varphi_H = 30°$ (blue curve). (b) Co S_{21} attenuation at 1 GHz for several angles between the SAW and the magnetic field. Co shows absorption when the SAW and the magnetic field are at an angle between −30° and 30°. The insets show a horizontal cut of S_{21} for $\varphi_H = 40°$ (black curve) and $\varphi_H = 30°$ (blue curve).

between opposite magnetizations can be directly linked to the M_s component in the direction of the x rays.

A. MAWs in nickel

The Ni sample was studied for two SAW frequencies: 1 and 3 GHz. Figures 3(a) and 3(b) show two-phase XMCD images

TABLE I. Amplitudes of the SAW strain components for each sample and SAW frequency corresponding to the Vpp values obtained from the secondary photoelectron energy spectra.

Sample	$V_{pp}(V)$	$e_{xx}(10^{-5})$	$e_{xy}(10^{-5})$	$e_{zz}(10^{-5})$
Ni (1 GHz)	0.90	14.3	2.95	4.23
Ni (3 GHz)	0.40	19.0	3.93	5.64
Co (1 GHz)	1.05	16.6	3.44	4.93

of excitations of both signals (1 and 3 GHz, respectively). The bottom part of the images corresponds to LiNbO$_3$ and displays the SAWs and the top part corresponds to Ni and shows the MAWs as indicated. Both images are taken with the same field-of-view (20×20 μm) and the same color scale to be able to distinguish the wavelength and the contrast difference. Figure 3(c) shows the MAW profile of both frequencies with their corresponding sinusoidal fit to show the large difference in amplitude (as well as the difference in wavelength). The sinusoidal fits use the amplitude and phase as fitting parameters, while the 1 GHz/3 GHz SAW excitation gives the frequency (and the wavelength). A summary of the normalized MAW amplitudes at different magnetic fields is presented in Fig. 3(d) for 1 GHz (black symbols, left axis) and 3 GHz (orange symbols, right axis). The overall magnetization precession amplitude at 1 GHz is one order of magnitude larger than that of 3 GHz, while the measured strain amplitude at the substrate was similar for the two frequencies; this will be explored in more detail in Sec. IV.

B. MAWs in cobalt

The Co sample was only studied at 1 GHz. Figure 4(a) displays a representative two-phase XMCD image with a field of view of 50×50 μm, where clear SAWs in LiNbO$_3$ and MAWs can be observed in Co at 1 GHz. The profile of this MAW is shown in Fig. 4(b) with the corresponding sinusoidal fit. Figure 4(c) collects results from different magnetic field values, without a clear trend but with different amplitudes for opposite magnetic field directions. This nonreciprocal behavior was seen as well in the SAW attenuation measurements shown in Fig. 2(b). We notice here that the studied range of fields is small and one may hint at a slight amplitude increase close to $\mu_0 H = \pm 7$ mT. The amplitude of the MAW is two orders of magnitude smaller than Ni at 1 GHz (and even one order smaller than Ni at 3 GHz). We notice here that in both experiments the applied magnetic field formed an angle of ∼45° with respect to the SAWs which could be outside the region of resonant coupling for Co [see Fig. 2(b)]; we will discuss it in Sec. IV.

IV. DISCUSSION

The experimental techniques employed here measured different quantities; a-FMR determines the attenuation of SAW energy under MAW resonance, while XMCD is a direct representation of the magnetization dynamics in the ferromagnetic film. By comparing our results with micromagnetic simulations, we can determine the efficiency of converting strain into a magnetization variation, thus obtaining the magnetoelastic constants.

The experimental results demonstrate a notable consistency in the behavior of Ni and Co at 1 GHz in both a-FMR and XMCD. Starting with Ni, when placed under a magnetic field at $\varphi_H = 45°$ relative to the SAWs, the effect of the ME coupling is the strongest at approximately ± 4 mT and it decays as the magnetic field strength increases. In the case of Co, the magnetic field that we could apply in XMCD imaging did not exceed 7 mT, limiting our knowledge at higher fields. However, a peak close to 5 mT is observed
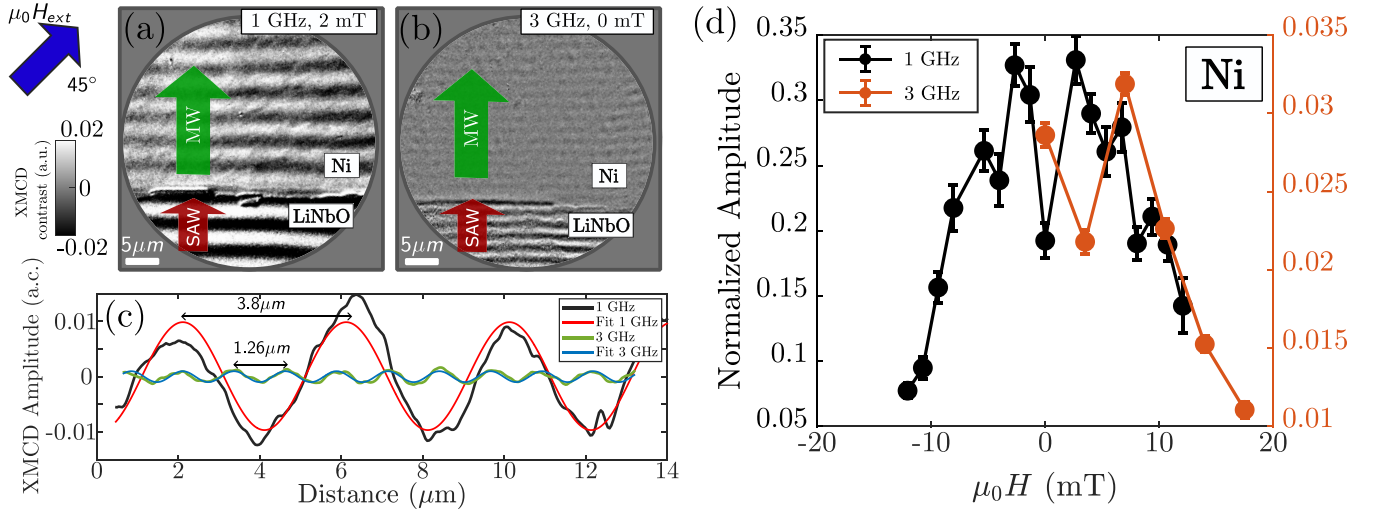
FIG. 3. (a) Two-phase XMCD image of Ni showing the MAW driven at 1 GHz. (b) Two-phase XMCD image of Ni showing the MAW driven at 3 GHz. Both color scales of (a) and (b) are equal to visually see the difference in contrast and are expressed in XMCD contrast, which is the difference in absorption between light circularly polarized to the right or to the left. (c) Experimentally determined MAW profiles at 1 GHz (black curve) and 3 GHz (green curve). The red and blue curves are fittings to a sinusoidal function. (d) Dependence of the MAW amplitude on the external magnetic field. The left axis represents the excitation at 1 GHz, while the right axis represents the excitation at 3 GHz.

in both a-FMR and XMCD experiments, with a decrease in amplitude when approaching 0 mT. Note that the amplitude of the MAWs of Co is one and two orders of magnitude lower than Ni at 3 and 1 GHz, respectively (also seen in acoustic attenuation in Fig. 2). This phenomenon could be due to the
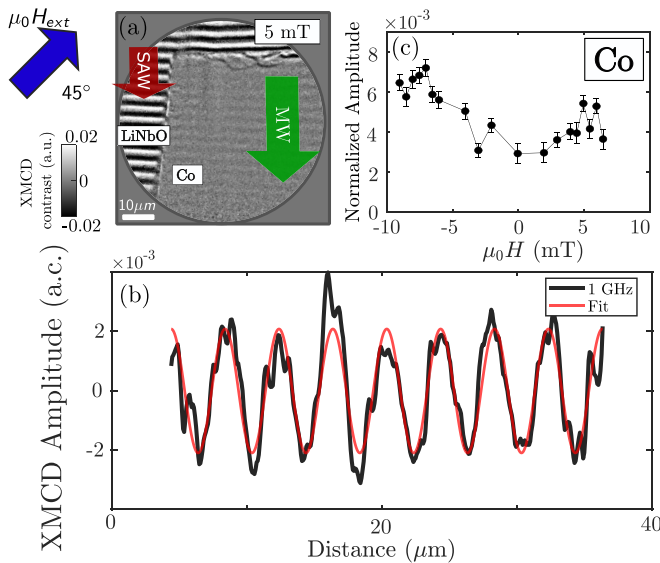

FIG. 4. (a) Two-phase XMCD image showing the piezoelectric, LiNbO$_3$, with visible SAWs and the ferromagnetic sample, Co, with visible MAWs at an applied magnetic field of 5 mT. The color scale represents the XMCD contrast, which is the difference in absorption between light circularly polarized to the right or to the left. (b) Experimentally determined MAW profile of the 5 mT XMCD image at 1 GHz excitation (black curve) with the corresponding sinusoidal fit (red curve). (c) MAW amplitude as a function of the applied magnetic field excited by a 1 GHz SAW.

high magnetization saturation of Co, which is three times larger than that of Ni. At 3 GHz frequency, the XMCD data of Ni display a trend with an applied magnetic field similar to that for the 1 GHz data, with a maximum of around 7 mT.

As discussed in Sec. III, we determined the strain amplitude for each frequency and sample using SAW XPEEM images on LiNbO$_3$ and employing the same power settings as in MAW imaging; see Table I. We observed similar relative values between the strain components for both samples at 1 GHz since identical IDTs were used on the same LiNbO$_3$ substrates. Notably, we also found that the strain at the sample surface measured at 3 GHz in the Ni sample was comparable and, even, slightly larger than those at 1 GHz. Therefore, the observed differences in the MAW amplitudes cannot be explained with strain values.

We performed micromagnetic simulations to evaluate the overall internal magnetic fields and determine the expected MAW amplitudes at each frequency for both materials. We used MuMax3 [41], which takes into account different magnetic contributions to the free energy, e.g., Zeeman, dipolar, exchange, and magnetoelastic to calculate an effective magnetic field. The effect of each contribution depends on the parameters of the experiment (SAW frequency and wavelength, external magnetic field, and magnetization saturation). In particular, for the ME contribution, the following free-energy expression is used:

$$F_{\mathrm{me}} = B_1\left[\varepsilon_{xx}m_x^2 + \varepsilon_{yy}m_y^2 + \varepsilon_{zz}m_z^2\right]$$
$$+ 2B_2[\varepsilon_{xy}m_xm_y + \varepsilon_{xz}m_xm_z + \varepsilon_{yz}m_ym_z], \quad (1)$$

where B_1 and B_2 are the magnetoelastic constants and are taken as parameters in our simulations, m_i are the normalized magnetization components, and ε_{ij} are the strain components simulated as plane waves with the following expression:

$$\varepsilon_{ij} = e_{ij}\exp\{i(kx - \omega t)\}, \quad (2)$$

TABLE II. Sample properties used in the micromagnetic simulations. M_s is the saturation magnetization, A_{ex} the exchange, and α the Gilbert damping.

Sample	M_s (kA/m)	A_{ex}(J/m)	α
Ni	490	10^{-11}	0.03
Co	1510	10^{-11}	0.007

where e_{ij} are the strain amplitudes of Table I, k is the wave vector of the SAW traveling in the x direction, and $\omega = 2\pi f$ is the angular frequency of the SAWs. Since the SAW excited in the LiNbO$_3$ substrate is a Rayleigh mode, only the strain amplitudes e_{xx}, e_{zz}, and e_{xz} are nonzero in our experiment. For the magnetic anisotropy we considered the following expression for the free energy:

$$F_{\text{anis}} = -K_{\text{u1}}(\mathbf{u} \cdot \mathbf{m})^2, \qquad (3)$$

where K_{u1} is the first order uniaxial anisotropy constant and $\mathbf{u}$ is the anisotropy direction. (See Table IV.)

The simulations consist of sweeping the magnetic field gradually from 20 to 0 mT, mirroring the experimental procedure, and recording the magnetization values in time and space in the presence of SAW. The choice of larger to lower magnetic fields is made to avoid magnetic switching and the formation of magnetic domains. The simulation parameters of each material are shown in Table II. Figure 5 shows the amplitude of the MAWs determined by calculating the mean oscillating amplitude over time for each magnetic field [42].

The results for Ni with SAW at 1 GHz and 3 GHz are presented in Fig. 5(a). The black curves depict simulations at 1 GHz considering no anisotropy (continuous line) and a small in-plane anisotropy of 1 mT in the x direction. Both curves have similar amplitudes with a clear decay when increasing field. The curve without anisotropy has a large increase at zero applied field because the sample's effective field also tends to zero, which is unrealistic. Therefore, we include a small in-plane uniaxial anisotropy field to better reproduce our experiments (black and orange dots in the graph). The simulations that better adjust to the experimental data correspond to a magnetoelastic constant of $B_1 = 11$ MJ/m^3 and a magnetic anisotropy of $K_{\text{u1}} = 1$ mT. The orange curves correspond to the 3 GHz simulations with the same conditions of anisotropy. In this case, the simulations with a magnetoelastic constant of about $B_1 = 0.3$ MJ/m^3 (and the same magnetic anisotropy, $K_{\text{u1}} = 1$ mT) are the ones most accurately matching the experimental results. The magnetoelastic constant is over 30 times smaller for 3 GHz compared with 1 GHz. Simulations show that the amplitude of MAW is proportional to the magnetoelastic constant in the range of $2 - 11$ MJ/m^3. An additional figure showing this effect and the effect of a magnetic anisotropy can be seen in Supplemental Material [43].

Figure 5(b) illustrates the simulated curves for the MAW amplitude of the Co sample when subjected to a 1 GHz excitation. Here we plot different angles, φ_H, between the applied field and SAW propagation, ranging from 10° to 40° (from blue to green curves) to show the huge decay of the MAW amplitude with increasing the angle [as shown in SAW
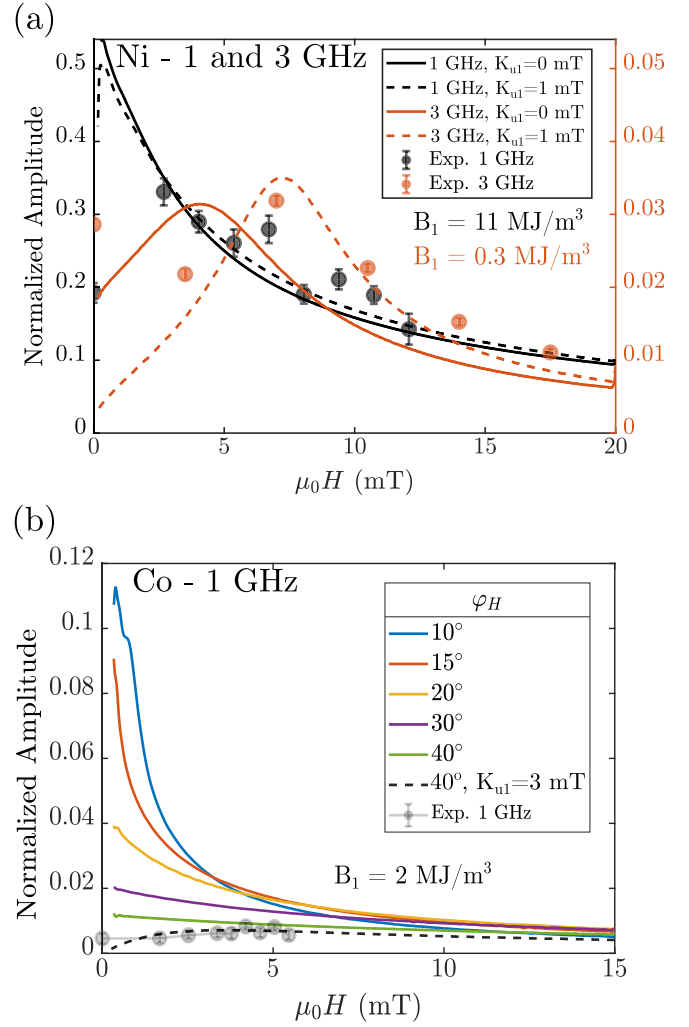

FIG. 5. Results of simulations. (a) Amplitude of MAW in Ni for excitation frequencies of 1 and 3 GHz with $\varphi_H = 45°$ (solid black and orange curves, respectively). The dashed lines provide the same information including a small anisotropy, $K_{\text{u1}} = 1$ mT. The magnetoelastic constants used for each frequency are written in the same color as the simulation curves. The faint black and orange dots are the experimental results. (b) Amplitude of the MAW in Co for an excitation frequency of 1 GHz at several φ_H, from 10° to 40°. The dashed black line represents the simulation at 40° with a small anisotropy, $K_{\text{u1}} = 3$ mT, while the faint black dots correspond to the experimental results.

attenuation, Fig. 2(b)]. The misalignment between MAW and applied field has a more drastic impact on Co reducing the overall MAW amplitude. This occurs because the resonant frequency is shifted above the SAW frequency as $\varphi_H > 10°$, resulting in no resonance. This same behavior is displayed in the a-FMR experiment (see Fig. 2). A curve for $\varphi_H = 40°$ and an in-plane anisotropy of 3 mT in the x direction is added with black dashed lines, showing, as in the case of Ni, an additional decay at zero field. The value for the magnetoelastic constant that adjusts better the simulations to the experimental data (gray dots in the graph) corresponds to a $B_1 = 2$ MJ/m^3 (see Table III).

TABLE III. Magnetoelastic constant values for each sample obtained through the simulations.

Sample	B_1 (MJ/m^3)
Ni (1 GHz)	11
Ni (3 GHz)	0.3
Co (1 GHz)	2

We now focus on the experimental results showing a drop in efficiency at 3 GHz for Ni (see Fig. 3). To account for the lower MAW amplitude, we varied the magnetoelastic constant, B_1, until the MAW amplitude matched the experimental values. For a 1 GHz excitation, a magnetoelastic constant of $B_1 = 11$ MJ/m^3 matched the experimental amplitude, while for a 3 GHz excitation, a reduced magnetoelastic constant of $B_1 = 0.3$ MJ/m^3 was needed to reproduce the experimental results. This loss in magnetoelastic energy appeared unexpected to us, given that experiments are done in the same Ni layer and that physical processes involved in magnetoelasticity are expected to respond easily at the nanosecond scale. We notice that the measured strain amplitudes were obtained at the piezoelectric surface and not at the ferromagnetic film. It could be possible that the reduced magnetic response at 3 GHz is related to a lower transmission of the SAW strain to the polycrystalline thin layer under high SAW frequencies and short wavelengths. We measured AFM in our Ni films and the observed grains at the top of the film were smaller than a few tens of nanometers, a value much shorter than the SAW wavelengths used in our experiment. However, the interface between LiNbO$_3$ and Ni has not been characterized.

Overall, the results of our simulations agree quantitatively well with the XMCD and a-FMR experiments for both Ni and Co. At 1 GHz SAW excitation we obtained a value of B_1 for Ni of ~ 11 MJ/m^3, which is slightly larger than previous experimental studies [15,28,44–46]. In Co, we obtained a magnetoelastic constant of ~ 2 MJ/m^3, which is over 4–5 times smaller than the Ni one at 1 GHz (and also up to 8 times smaller if compared to the bulk value [47]). However, the simulations indicate that Co at smaller angles may achieve amplitudes approximately equal to 0.1, comparable to Ni, which could make Co an interesting material for straintronics, due to its low damping and high magnetization saturation. At 3 GHz SAW excitation, we found a reduction in the amplitude

of the MAWs in Ni that requires decreasing the magnetoelastic constant (to ~ 0.3 MJ/m^3) approximately a factor of 30 compared to 1 GHz excitation. Although our model does not account for the direct transfer of the phonon angular momentum to magnetization [34,48], which might be dependent on frequency, we consider that a plausible explanation for the drop in efficiency at 3 GHz could be related to a frequency dependence of the strain transfer efficiency between LiNbO$_3$ and the Ni film.

V. CONCLUSIONS

We have studied the magnetoelastic effect in Ni and Co at 1 and 3 GHz using hybrid piezoelectric/ferromagnetic devices and SAWs. Our direct XPEEM-XMCD imaging shows that large amplitude MAWs in Ni and Co at frequencies of 1 and 3 GHz can be directly imaged and quantified. We found a significant difference in MAW amplitude between Ni and Co at 1 GHz excitations—a difference that cannot be explained only by the larger magnetization saturation value of Co compared with the value of Ni. Thus a lower magnetoelastic constant is obtained for Co. The found values for the magnetoelastic constants at 1 GHz are similar to those reported in the literature [15,28,44–46]. Additional measurements at 3 GHz SAW excitations show a clear decay in MAW efficiency suggesting a drop in the phonon coupling between SAW at the piezoelectric substrate and SAW at the ferromagnetic thin film. Our study provides valuable insights into the coupling between strain and magnetization dynamics at the GHz frequency and may guide the development of more efficient acoustic spintronic (straintronic) devices.

[1] N. Locatelli, V. Cros, and J. Grollier, Spin-torque building blocks, Nat. Mater. **13**, 11 (2014).

[2] D. Ralph and M. Stiles, Spin transfer torques, J. Magn. Magn. Mater. **320**, 1190 (2008).

[3] A. Brataas, A. D. Kent, and H. Ohno, Current-induced torques in magnetic materials, Nat. Mater. **11**, 372 (2012).

[4] A. A. Bukharaev, A. K. Zvezdin, A. P. Pyatakov, and Y. K. Fetisov, Straintronics: A new trend in micro- and nanoelectronics and materials science, Phys. Usp. **61**, 1175 (2018).

[5] M. Foerster and F. Macià, Preface to special issue on magneto-elastic effects, J. Phys.: Condens. Matter **31**, 190301 (2019).

[6] C.-H. Lambert, S. Mangin, B. S. D. C. S. Varaprasad, Y. K. Takahashi, M. Hehn, M. Cinchetti, G. Malinowski, K. Hono, Y. Fainman, M. Aeschlimann, and E. E. Fullerton, All-optical control of ferromagnetic thin films and nanostructures, Science **345**, 1337 (2014).

[7] M. Barangi and P. Mazumder, Straintronics: A leap toward ultimate energy efficiency of magnetic random access memories, IEEE Nanotechnol. Mag. **9**, 15 (2015).

[8] Z. Wang, Y. Zhang, Y. Wang, Y. Li, H. Luo, J. Li, and D. Viehland, Magnetoelectric assisted 180° magnetization switching for electric field addressable writing in magnetoresistive random-access memory, ACS Nano **8**, 7793 (2014).

[9] H. B. Huang, J. M. Hu, T. N. Yang, X. Q. Ma, and L. Q. Chen, Strain-assisted current-induced magnetization reversal in magnetic tunnel junctions: A micromagnetic study with phase-field microelasticity, Appl. Phys. Lett. **105**, 122407 (2014).

[10] J. Cenker, S. Sivakumar, K. Xie, A. Miller, P. Thijssen, Z. Liu, A. Dismukes, J. Fonseca, E. Anderson, X. Zhu, X. Roy, D. Xiao, J.-H. Chu, T. Cao, and X. Xu, Reversible strain-induced magnetic phase transition in a van der Waals magnet, Nat. Nanotechnol. **17**, 256 (2022).

[11] A. K. Ganguly, K. L. Davis, D. C. Webb, and C. Vittoria, Magnetoelastic surface waves in a magnetic film–piezoelectric substrate configuration, J. Appl. Phys. **47**, 2696 (1976).

[12] I.-a. Feng, M. Tachiki, C. Krischer, and M. Levy, Mechanism for the interaction of surface waves with 200-Å nickel films, J. Appl. Phys. **53**, 177 (1982).

[13] W.-G. Yang and H. Schmidt, Acoustic control of magnetism toward energy-efficient applications, Appl. Phys. Rev. **8**, 021304 (2021).

[14] J. Puebla, Y. Hwang, S. Maekawa, and Y. Otani, Perspectives on spintronics with surface acoustic waves, Appl. Phys. Lett. **120**, 220502 (2022).

[15] B. Casals, N. Statuto, M. Foerster, A. Hernández-Mínguez, R. Cichelero, P. Manshausen, A. Mandziak, L. Aballe, J. M. Hernández, and F. Macià, Generation and imaging of magnetoacoustic waves over millimeter distances, Phys. Rev. Lett. **124**, 137202 (2020).

[16] M. Weiler, L. Dreher, C. Heeg, H. Huebl, R. Gross, M. S. Brandt, and S. T. B. Goennenwein, Elastically driven ferromagnetic resonance in nickel thin films, Phys. Rev. Lett. **106**, 117601 (2011).

[17] P. G. Gowtham, T. Moriyama, D. C. Ralph, and R. A. Buhrman, Traveling surface spin-wave resonance spectroscopy using surface acoustic waves, J. Appl. Phys. **118**, 233910 (2015).

[18] D. Labanowski, A. Jung, and S. Salahuddin, Power absorption in acoustically driven ferromagnetic resonance, Appl. Phys. Lett. **108**, 022905 (2016).

[19] K. M. Seemann, O. Gomonay, Y. Mokrousov, A. Hörner, S. Valencia, P. Klamser, F. Kronast, A. Erb, A. T. Hindmarch, A. Wixforth, C. H. Marrows, and P. Fischer, Magnetoelastic resonance as a probe for exchange springs at antiferromagnet-ferromagnet interfaces, Phys. Rev. B **105**, 144432 (2022).

[20] P. Kuszewski, I. S. Camara, N. Biarrotte, L. Becerra, J. von Bardeleben, W. S. Torres, A. Lemaître, C. Gourdon, J.-Y. Duquesne, and L. Thevenard, Resonant magneto-acoustic switching: influence of rayleigh wave frequency and wavevector, J. Phys.: Condens. Matter **30**, 244003 (2018).

[21] C. Müller, P. Durdaut, R. B. Holländer, A. Kittmann, V. Schell, D. Meyners, M. Höft, E. Quandt, and J. McCord, Imaging of love waves and their interaction with magnetic domain walls in magnetoelectric magnetic field sensors, Adv. Electron. Mater. **8**, 2200033 (2022).

[22] M. Rovirola, M. Waqas Khaliq, B. Casals, M. Foerster, M. A. Niño, L. Aballe, J. Herfort, J. M. Hernàndez, F. Macià, and A. Hernández-Mínguez, Resonant and off-resonant magnetoacoustic waves in epitaxial Fe$_3$Si/GaAs hybrid structures, Phys. Rev. Appl. **20**, 034052 (2023).

[23] M. W. Khaliq, O. Amin, A. Hernández-Mínguez, M. Rovirola, B. Casals, K. Omari, S. Ruiz-Gómez, S. Finizio, R. P. Campion, K. W. Edmonds, V. Novak, A. Mandziak, L. Aballe, M. A. Niño, J. M. Hernàndez, P. Wadley, F. Macià, and M. Foerster,

Magneto-acoustic waves in antiferromagnetic CuMnAs excited by surface acoustic waves, arXiv:2309.08893.

[24] R. M. White and F. W. Voltmer, Direct piezoelectric coupling to surface elastic waves, Appl. Phys. Lett. **7**, 314 (1965).

[25] P. Delsing, A. N. Cleland, M. J. A. Schuetz, J. Knörzer, G. Giedke, J. I. Cirac, K. Srinivasan, M. Wu, K. C. Balram, C. Bäuerle, T. Meunier, C. J. B. Ford, P. V. Santos, E. Cerda-Méndez, H. Wang, H. J. Krenner, E. D. S. Nysten, M. Weiß, G. R. Nash, L. Thevenard *et al.*, The 2019 surface acoustic waves roadmap, J. Phys. D **52**, 353001 (2019).

[26] D.-L. Zhang, J. Zhu, T. Qu, D. M. Lattery, R. H. Victora, X. Wang, and J.-P. Wang, High-frequency magnetoacoustic resonance through strain-spin coupling in perpendicular magnetic multilayers, Sci. Adv. **6**, eabb4607 (2020).

[27] H. Qin, R. B. Holländer, L. Flajšman, F. Hermann, R. Dreyer, G. Woltersdorf, and S. van Dijken, Nanoscale magnonic Fabry-Pérot resonator for low-loss spin-wave manipulation, Nat. Commun. **12**, 2293 (2021).

[28] M. Foerster, F. Macià, N. Statuto, S. Finizio, A. Hernández-Mínguez, S. Lendínez, P. V. Santos, J. Fontcuberta, J. M. Hernàndez, M. Kläui, and L. Aballe, Direct imaging of delayed magneto-dynamic modes induced by surface acoustic waves, Nat. Commun. **8**, 407 (2017).

[29] A. Slobodnik, Surface acoustic waves and saw materials, Proc. IEEE **64**, 581 (1976).

[30] L. Aballe, M. Foerster, E. Pellegrin, J. Nicolas, and S. Ferrer, The ALBA spectroscopic LEEM-PEEM experimental station: layout and performance, J. Synchrotron Radiat. **22**, 745 (2015).

[31] M. Foerster, N. Statuto, B. Casals, A. Hernández-Mínguez, R. Cichelero, P. Manshausen, A. Mandziak, L. Aballe, J. Hernández Ferràs, and F. Macià, Quantification of propagating and standing surface acoustic waves by stroboscopic x-ray photoemission electron microscopy, J. Synchrotron Radiat. **26**, 184 (2019).

[32] M. W. Khaliq, J. M. Álvarez, A. Camps, N. González, J. Ferrer, A. Martinez-Carboneres, J. Prat, S. Ruiz-Gómez, M. A. Niño, F. Macià, L. Aballe, and M. Foerster, Ghz sample excitation at the ALBA-PEEM, Ultramicroscopy **250**, 113757 (2023).

[33] L. Dreher, M. Weiler, M. Pernpeintner, H. Huebl, R. Gross, M. S. Brandt, and S. T. B. Goennenwein, Surface acoustic wave driven ferromagnetic resonance in nickel thin films: Theory and experiment, Phys. Rev. B **86**, 134415 (2012).

[34] J. Puebla, M. Xu, B. Rana, K. Yamamoto, S. Maekawa, and Y. Otani, Acoustic ferromagnetic resonance and spin pumping induced by surface acoustic waves, J. Phys. D **53**, 264002 (2020).

[35] M. Weiler, H. Huebl, F. S. Goerg, F. D. Czeschka, R. Gross, and S. T. B. Goennenwein, Spin pumping with coherent elastic waves, Phys. Rev. Lett. **108**, 176601 (2012).

[36] A. Hernández-Mínguez, F. Macià, J. M. Hernàndez, J. Herfort, and P. V. Santos, Large nonreciprocal propagation of surface acoustic waves in epitaxial ferromagnetic/semiconductor hybrid structures, Phys. Rev. Appl. **13**, 044018 (2020).

[37] M. Xu, K. Yamamoto, J. Puebla, K. Baumgaertl, B. Rana, K. Miura, H. Takahashi, D. Grundler, S. Maekawa, and Y. Otani, Nonreciprocal surface acoustic wave propagation via magneto-rotation coupling, Sci. Adv. **6**, eabb1724 (2020).

[38] P. J. Shah, D. A. Bas, I. Lisenkov, A. Matyushov, N. X. Sun, and M. R. Page, Giant nonreciprocity of surface acoustic waves

enabled by the magnetoelastic interaction, Sci. Adv. **6**, eabc5648 (2020).

[39] L. Rayleigh, On waves propagated along the plane surface of an elastic solid, Proc. London Math. Soc. **s1-17**, 4 (1885).

[40] B. A. Auld, Acoustic fields and waves in solids, *Acoustic Fields and Waves in Solids* (John Wiley and Sons, New York, 1973), Vol. 2.

[41] A. Vansteenkiste, J. Leliaert, M. Dvornik, M. Helsen, F. Garcia-Sanchez, and B. Van Waeyenberge, The design and verification of MuMax3, AIP Adv. **4**, 107133 (2014).

[42] See Supplemental Material at http://link.aps.org/supplemental/10.1103/PhysRevResearch.6.023285 for the micromagnetic simulation code.

[43] See Supplemental Material at http://link.aps.org/supplemental/10.1103/PhysRevResearch.6.023285 for the results on the effect of B1 and Ku1 in the micromagnetic simulations.

[44] O. Song, C. A. Ballentine, and R. C. O'Handley, Giant surface magnetostriction in polycrystalline Ni and NiFe films, Appl. Phys. Lett. **64**, 2593 (1994).

[45] B. Cullity and C. Graham, *Introduction to Magnetic Materials* (John Wiley & Sons, Ltd, New York, 2008), Chap. 8, pp. 241–273.

[46] X. Li, D. Labanowski, S. Salahuddin, and C. S. Lynch, Spin wave generation by surface acoustic waves, J. Appl. Phys. **122**, 043904 (2017).

[47] R. C. O'Handley, *Modern Magnetic Materials: Principles and Applications* (John Wiley & Sons, Ltd, New York, 2000).

[48] R. Sasaki, Y. Nii, and Y. Onose, Magnetization control by angular momentum transfer from surface acoustic wave to ferromagnetic spin moments, Nat. Commun. **12**, 2599 (2021).